PAPER

CrossMark
←click for updates

The effects of globotriaosylceramide tail saturation level on bilayer phases†

Weria Pezeshkian,[ab] Vitaly V. Chaban,[a] Ludger Johannes,[c] Julian Shillcock,[d] John H. Ipsen[a] and Himanshu Khandelia*[a]

Globotriaosylceramide (Gb$_3$) is a glycosphingolipid present in the plasma membrane that is the natural receptor of the bacterial Shiga toxin. The unsaturation level of Gb$_3$ acyl chains has a drastic impact on lipid bilayer properties and phase behaviour, and on many Gb$_3$-related cellular processes. For example: the Shiga toxin B subunit forms tubular invaginations in the presence of Gb$_3$ with an unsaturated acyl chain (U-Gb$_3$), while in the presence of Gb$_3$ with a saturated acyl chain (S-Gb$_3$) such invagination does not occur. We have used all-atom molecular dynamics simulations to investigate the effects of the Gb$_3$ concentration and its acyl chain saturation on the phase behaviour of a mixed bilayer of dioleoylphosphatidylcholine and Gb$_3$. The simulation results show that: (1) the Gb$_3$ acyl chains (longer tails) from one leaflet interdigitate into the opposing leaflet and lead to significant bilayer rigidification and immobilisation of the lipid tails. S-Gb$_3$ can form a highly ordered, relatively immobile phase which is resistant to bending while these changes for U-Gb$_3$ are not significant. (2) At low concentrations of Gb$_3$, U-Gb$_3$ and S-Gb$_3$ have a similar impact on the bilayer reminiscent of the effect of sphingomyelin lipids and (3) At higher Gb$_3$ concentrations, U-Gb$_3$ mixes better with dioleoylphosphatidylcholine than S-Gb$_3$. Our simulations also provide the first molecular level structural model of Gb$_3$ in membranes.

Introduction

Glycosphingolipids (GSLs) are a class of lipids consisting of a ceramide linked to a carbohydrate moiety and are abundant in the outer leaflet of the plasma membrane. They are involved in many biological processes including macromolecular recognition, intracellular protein uptake and cell adhesion (reviewed in ref. 1). Globotriaosylceramide (Gb$_3$) is an interesting GSL lipid which is required for the binding of Shiga toxin to the host cell membrane and the toxin's subsequent internalization into the cell.[2,3] Gb$_3$ is over-expressed in metastatic colon cancer and its presence is sufficient for epithelial cells to be invasive.[4] The high expression of Gb$_3$ in invasive colon cancer cells suggests a possible route to target and detect these cells.[4,5] The Gb$_3$-binding B-subunit of Shiga toxin (STxB) has also been used to target defined antigens to dendritic cells for the induction of a

therapeutic immune response against cancer or intracellular pathogens.[6–8]

STxB binds up to 15 Gb$_3$ lipids on the surface of the host cell membrane[9] and allows the intracellular transport of the toxin via the retrograde route.[2] STxB can also bind to, aggregate and form clusters on model membranes composed of dioleoylphosphatidylcholine (DOPC) and porcine Gb$_3$, and if the membrane tension is sufficiently low, it drives the model membrane to invaginate and form tubular invaginations.[2,10–12] The Gb$_3$ lipid is a large and chemically diverse molecule. It contains three sugar moieties, αGal(1–4) βGal(1–4) βGlc, which are connected to a ceramide. The acyl chain structure of this ceramide varies in different Gb$_3$ species and the saturation level of this acyl chain affects many Gb$_3$ involving processes. For example binding of STxB to a bilayer composed of dioleoylphosphatidylcholine (DOPC) and Gb$_3$ with saturated acyl chains does not lead to the formation of tubular invaginations, whereas invagination occurs for unsaturated Gb$_3$.[2,11,13,14] Also, a lipid bilayer containing DOPC, sphingomyelin, cholesterol and Gb$_3$ phase separate into a liquid ordered (l$_o$) and a liquid disordered (l$_d$) phase at room temperature. Phase behaviour of such a bilayer is strongly influenced by STxB clustering as well as the saturation levels and length of the Gb$_3$ fatty acyl chain.[11,13,15] Recently, the condensation of phospholipid–Gb$_3$ monolayers was studied, using X-ray reflectivity and grazing incidence X-ray diffraction. The capacity of Gb$_3$ to condense the monolayers was strongly affected by unsaturation levels of its acyl chain.[16]

[a] Center for Biomembrane Physics (MEMPHYS), Department of Physics, Chemistry and Pharmacy (FKF), University of Southern Denmark, Campusvej 55, 5230 Odense M, Denmark. E-mail: hkhandel@sdu.dk

[b] TRANSPOL Molecular Neurobiochemistry, RUHR UNIVERSITAT BOCHUM, Bochum, Germany

[c] U1143 INSERM-UMR3666 CNRS, Institut Curie, 26 Rue DUlm, 75248 Paris Cedex 05, France

[d] Ecole Polytechnique Fèdèrale De Lausanne (EPFL), 1015 Lausanne, Switzerland

† Electronic supplementary information (ESI) available. See DOI: 10.1039/c4sm02456g

Despite the important cellular roles of Gb$_3$ and its significant impact on the physical behaviour of the lipid bilayers, it has not been studied by simulations before. Therefore, we use all-atom MD simulations to investigate a mixed bilayer of DOPC and Gb$_3$ with two different acyl chain compositions, Gb$_3$-22 : 0 (Gb$_3$ with a saturated acyl chain with 22 carbon atoms) and Gb$_3$-22 : 1 (Gb$_3$ with an unsaturated acyl chain with 22 carbon atoms and a trans-double bound in C$_{13}$–C$_{14}$). We refer to the saturated and unsaturated versions of Gb$_3$ as S-Gb$_3$ and U-Gb$_3$, respectively. The simulations reveal two important features of the Gb$_3$ structure which strongly affect lipid bilayer physical properties. First: Gb$_3$ fatty acyl chains from one leaflet interdigitate into the opposite monolayer leading to a reduction in chain fluctuations, ordering of all fatty acyl chains in the bilayer and result in a bilayer with higher bending resistance. Second: the degree of the Gb$_3$ acyl chain saturation influences the phase behaviour of the bilayer where for fully saturated acyl chains an ordered phase was observed. Our simulations can explain several experimental observable processes, which we present in the Discussion section of the report.

Methods, force field and systems

Methods

We performed all-atom MD simulations of mixtures of DOPC and Gb$_3$ lipids using GROMACS[17–20] software and the CHARMM36 force field (FF).[21,22] The Gb$_3$ molecule had a C$_{18}$ sphingosine tail and either a 22 : 0 acyl tail (S-Gb$_3$) or a 22 : 1 acyl tail unsaturated at C$_{13}$ (U-Gb$_3$). For all systems, at least 100 water molecules (The TIP3P solvent model[23]) per lipid were present (some simulations were repeated using the TIPS3P water model,[24] and the differences in the results were within the range of error bars). Na and Cl ions corresponding to a biological concentration of 150 mmol were present. Electrostatic interactions were treated with particle-mesh Ewald (PME) with a short range cutoff 1.2 nm, and van der Waals interactions were switched off between 1.0 and 1.2 nm. The system temperature was kept constant at 37 °C using Nose–Hoover temperature coupling.[25,26] Bonds containing hydrogen atoms were constrained using the LINCS algorithm.[27] Parrinello–Rahman barostat pressure coupling[28,29] was applied on all systems after equilibrating the systems with Berendsen pressure coupling.[30] The leap frog integrator was used with a timestep of 2 fs.

Force field parameters for Gb$_3$

The Gb$_3$ lipid contains three sugar moieties, αGal(1–4), βGal(1–4) and βGlc (Blue segment of Fig. 1A), which are connected to ceramide. The sugar moiety was described by the CHARMM36 FF for carbohydrates.[31–35] Point electrostatic charges needed for HO–CH$_2$–CH–CH–CH$_2$–... (Green segment of Fig. 1A) are not provided in the CHARMM36 FF. As point electrostatic charges are unknown for the HO–CH$_2$–CH–CH–CH$_2$–... moiety of Gb$_3$, we have performed electronic structure calculations for a set of similar systems to obtain information on the electron density distribution. All-electron Möller–Plesset second-order perturbation theory, MP2, was used. The wave function was
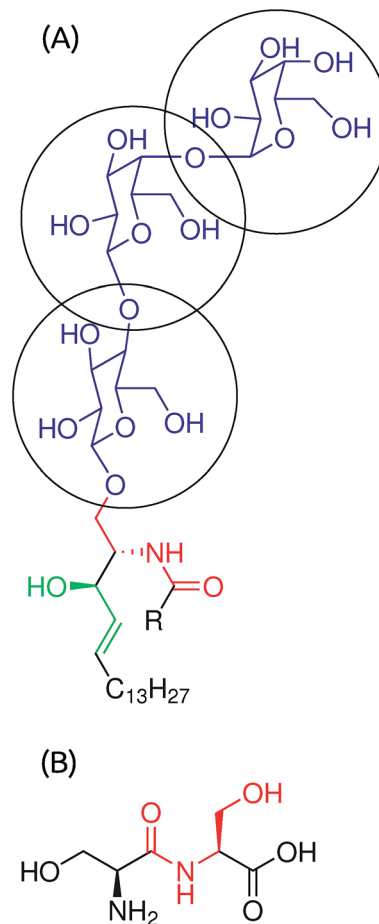

Fig. 1 (A) Molecular structure of a Gb$_3$ lipid. The acyl chain has 22 carbon atoms and it could be saturated (S-Gb$_3$) or with a double bond between carbons 13 and 14 of the acyl chain (U-Gb$_3$). (B) A serine–serine peptide bond.

constructed using the 6-311G basis set. Polarization and diffuse functions were added to this basis set. Additionally, polarization and diffuse functions were added to all hydrogen atoms. A strict self-consistent field convergence criterion of 10−9 Ha was applied. Geometries of the molecules were optimized at the same level of theory prior to the computation of the electrostatic potential (ESP). The ESP, derived from the electronic structure, was reproduced using a set of point charges centered on each atom, including hydrogen atoms. The atom spheres were defined according to the CHELPG scheme.[36] The calculations were performed using the GAUSSIAN 09 program.[37] We considered 4 model compounds, (1) CH$_2$=CH–CH$_2$–OH, (2) CH$_3$–CH$_2$–CH$_2$–OH, (3) CH$_3$–CH=CH–CH$_3$ and (4) CH$_3$–CH=CH–CH$_2$–OH. The inclusion of enumerated compounds into consideration was necessary to ensure reasonable transferability of the assigned charges. Please refer to the ESI† for a more detailed description of the development of the force field. The derived charges are summarized in Table 1. The HO–CH$_2$–CH–NH–C=O moiety (Red segment of Fig. 1A and B) was described using serine–serine peptide bond parameters in the CHARMM36 FF for proteins. Finally, the fatty acid chains were described by the CHARMM36 FF for lipids.

Table 1 Extracted point charges using quantum calculation for structure HO−OH−αCH^1−βCH^2=γCH^3

Atoms	Charge
OH	−0.70
HO	+0.40
αC	+0.55
H^1	−0.05
βC	−0.30
H^2	+0.10
γC	−0.10
H^3	+0.10

Simulated systems

Details of all simulated systems are present in Table 2. Five different Gb$_3$ concentrations in a DOPC bilayer, 0, 12, 25, 50, and 100 percent, were simulated. Two extra simulations to investigate the phase separation tendency of Gb$_3$ were performed (Table 2). For systems 1–9, initial configurations were built by placing all DOPC lipids on a lattice and then a sufficient amount of the DOPC lipids was randomly replaced by Gb$_3$ lipids to the desired concentration. The number of Gb$_3$ lipids in both the monolayers is equal. For Gb$_3$ domain simulations (systems 10 and 11), 16 DOPC lipids were replaced by 16 Gb$_3$ lipids in the middle of the upper mono-layer of the bilayer.

Results

The last 200 ns of the simulation outputs were used for data analysis. We performed an initial check on our simulation methodology by measuring the structural properties of a pure DOPC bilayer, and found that they are in good agreement with previous results from experiments and other simulations. In particular, the area per lipid and bilayer thickness were 64.7 ± 1.2 Å^2 and 36.4 ± 0.6 Å, which are close to the literature results of 68.0 Å^2 and 36.6 Å (ref. 38) extracted from simulations. Experimental values are 67.4 Å^2 (ref. 39) for the area per lipids and 36.1, 36.7 and 37.6 at 45, 30, and 15 °C,[40,41] respectively for the membrane thickness. The area and thickness are the two key mechanical properties that characterise a planar bilayer. The area per lipid responds sensitively to the lipid phase, and

the thickness influences the membrane curvature modulus that governs its thermal fluctuations. Our results show that these mechanical properties strongly depend on the membrane composition and the structural details of the Gb$_3$ acyl chains.

The rest of the paper is organized as follows. First, we report on the area and thickness using several different techniques for accurate measurement of the area per molecule. We then explore the influence of the Gb$_3$ on the membrane dynamical properties, and measure the lipid tail order parameters, fatty acid tilt distributions, lipid diffusion, rotational correlation times and the tendency of Gb$_3$ to phase separate. All of these properties are found to be sensitive to the Gb$_3$ concentrations and the degree of Gb$_3$ acyl chain saturation. In the Discussion section, we elaborate upon the main findings, and show how the simulations explain several previously unexplained experimental observations with regard to membrane invagination induced by Shiga toxins and the phase behaviour induced by Gb$_3$.

Area per lipid and membrane thickness

We used three different methods to calculate the area per lipid.

Projected area per lipid(a_p), calculated from box size. For a one-component flat bilayer, the area per lipid is equal to $a_p = 2L_xL_y/N$ where L_x and L_y are the simulation box dimensions in the plane of the bilayer and N is the number of the lipids in the system. Fig. 3 shows a_p as a function of time for different systems. The time average of a_p is presented in Table 3, column 2.

Projected area per lipid, calculated by Voronoi tessellation(a_v). To obtain the individual area per lipid values in a mixed bilayer, we used Voronoi tessellation. The APL@Voro software was used.[42] The data for this method are presented in Table 3, column 3.

Polynomial fitting. For a curved bilayer, neither of the previous methods can give an accurate value of the area per lipid. Instead, a polynomial fit to the membrane surface gives a better estimate of the area. Additionally, this method can be used to calculate the curvature and membrane thickness profile. A functional form for the bilayer surface can be obtained by fitting a polynomial of degree s to the coordinates of specific

Table 2 List of implemented simulations

System	DOPC/Gb$_3$	Na/Cl	Solvent	Time (ns)
0% Gb$_3$	128/0	24/24	9088	380
12% U-Gb$_3$	176/24	37/37	13 689	320
12% S-Gb$_3$	176/24	36/36	13 625	330
25% U-Gb$_3$	96/32	25/25	9359	325
25% S-Gb$_3$	96/32	23/23	8784	250
50% U-Gb$_3$	64/64	19/19	7350	380
50% S-Gb$_3$	64/64	17/17	6354	520
100% U-Gb$_3$	0/128	45/45	17 671	200
100% S-Gb$_3$	0/128	36/36	13 611	200
U-Gb$_3$ domain	322/16	74/74	28 612	400
S-Gb$_3$ domain	322/16	62/62	23 735	400

Table 3 Area per lipid and bilayer thickness: (1) a_p is the projected area per lipid calculated from box dimensions, (2) a real area estimated from polynomial fitting, (3) a_v projected area calculated using Voroni tessellation and (4) bilayer thickness (L_m)

System	a_p (Å^2)	a (Å^2)	a_v (DOPC/Gb$_3$)	L_m (Å)
0 Gb$_3$	64.7 ± 1.2	65.3 ± 0.9	64.7/—	36.4 ± 0.6
12 S-Gb$_3$	61.6 ± 0.8	61.9 ± 0.7	62.9/54.8	38.9 ± 0.5
12 U-Gb$_3$	62.2 ± 0.8	62.9 ± 0.8	63.0/53.8	38.6 ± 0.5
25 S-Gb$_3$	59.2 ± 1.0	60.4 ± 0.7	61.1/53.7	38.2 ± 0.6
25 U-Gb$_3$	60.0 ± 1.0	61.7 ± 1.1	62.0/55.7	37.4 ± 0.5
50 S-Gb$_3$	47.2 ± 0.4	50.8 ± 1.2	49.3/45.6	43.1 ± 0.3
50 U-Gb$_3$	54.1 ± 1.0	55.0 ± 1.0	55.7/50.5	39.0 ± 0.5
100 U-Gb$_3$	53.2 ± 0.5	58.0 ± 1.0	—	—
100 S-Gb$_3$	52.6 ± 0.5	60.0 ± 1.0	—	—

atoms, such as the phosphorus atom in DOPC lipids in one monolayer (eqn (1)).

$$z(x, y) = \sum_{n,m=0}^{m+n \leq s} a_{(m,n)} x^m y^n \qquad (1)$$

where m and n are integer numbers and taking all values in the interval zero to $m + n \leq s$. $a_{(m,n)}$ are polynomial coefficients that are extracted from fitting. The area is evaluated as:

$$A = \int_0^{L_x} \int_0^{L_y} \left(1 + \left\langle z(x,y)_x \right\rangle_\tau^2 + \left\langle z(x,y)_y \right\rangle_\tau^2 \right)^{\frac{1}{2}} dx \, dy \qquad (2)$$

where $\langle A(x,y) \rangle_\tau$ is a time average of the function $A(x,y)$ in a specific time period, τ, (we have used $\tau = 20$ ns) that minimizes the effects of membrane protrusions and shape fluctuations due to thermal fluctuations. $z(x,y)_x$ and $z(x,y)_y$ are partial derivatives of the function $z(x,y)$ with respect to x and y, respectively. For most of the systems (except for pure U-Gb$_3$ or S-Gb$_3$) the polynomial method gives similar values for area per lipid as the previous methods (Table 3). However, for the pure systems, the polynomial method extracts a higher value for the area per lipid, indicating that the pure Gb$_3$ bilayers are not planar (Fig. 2C and D). In general, the increase in Gb$_3$ concentration results in decreases in area per lipid and tighter bilayer packing (a similar result was observed experimentally[16]). The decrease in the area per lipid comes from two sources: increase in the amount of Gb$_3$ which has a smaller area per lipid or a change in the membrane phase behaviour, from a disordered to an ordered phase. At low Gb$_3$ concentration, the first effect plays a major role, because the area per lipid (a_v) for Gb$_3$ remains constant while the a_v for DOPC changed because the number of the DOPC lipids in contact with Gb$_3$ increased. However, at high S-Gb$_3$ concentrations, the Gb$_3$ a_v is lowered significantly which indicates a change in the phase state of the bilayer. We will elaborate on this in the subsequent sections.

Bilayer thickness. We calculated membrane thickness as the distance between phosphorus atoms in the two monolayers (L_m) (Table 3, column 5). L_m does not change much for low Gb$_3$ concentrations, but for high S-Gb$_3$ concentrations, this value increases significantly (a similar conclusion was made using X-ray diffraction[16]). We did not report any value for 100% Gb$_3$ since it is not a planar bilayer.

Chain order parameter

The orientational order of lipid chains is described by a deuterium order parameter which is given as:

$$S_{CD} = \frac{1}{2} \left\langle 3 \cos^2 \theta - 1 \right\rangle \qquad (3)$$

where θ is the angle between the **C–H** vector and the bilayer normal.[43,44] The reported order parameters in Fig. 4 show that Gb$_3$ fatty acid chains are always more ordered compared to DOPC. Also, the Gb$_3$ sphingosine chain is more ordered than the Gb$_3$ acyl chain, which was also observed for sphingomyelin lipids in previous simulations.[45] DOPC chains became more ordered with increasing Gb$_3$ concentrations, because of unfavourable contacts of DOPC lipids with the Gb$_3$ lipids, which results in the decrease of the molecular volume of both DOPC and Gb$_3$. This effect is much stronger for S-Gb$_3$ because lipids with unsaturated acyl chains dissolve more easily into each other.
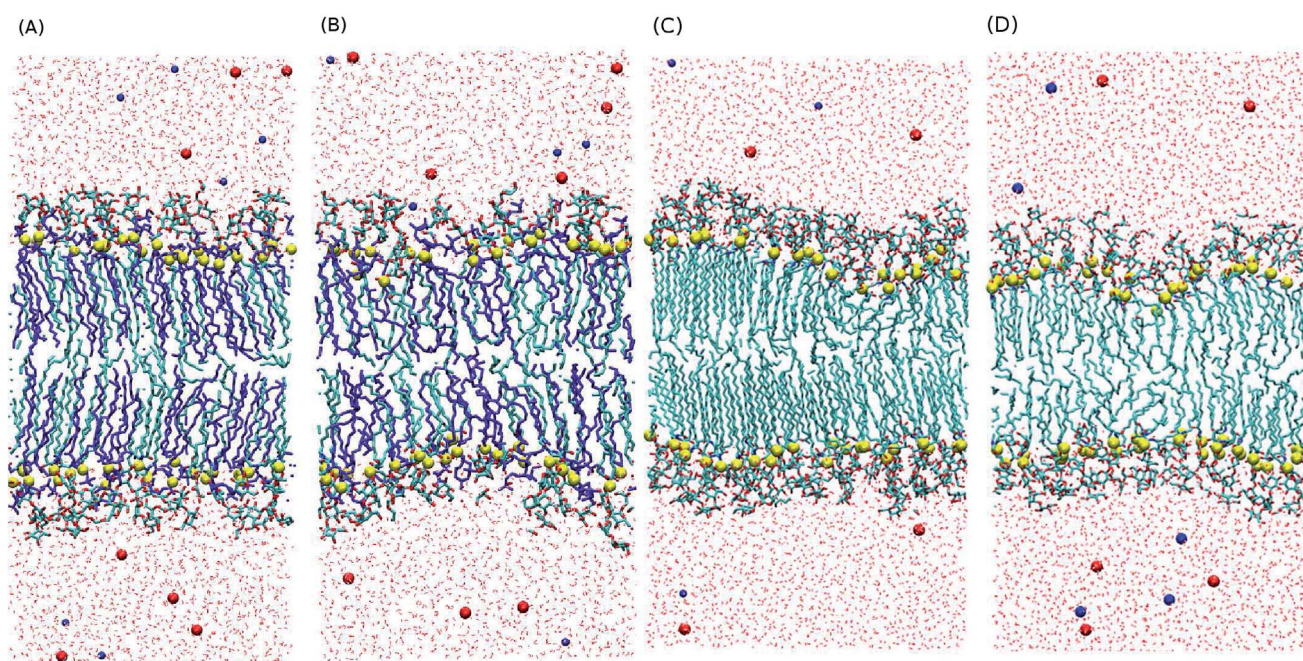

Fig. 2   Last snapshot of the system for (A) 50% S-Gb$_3$ (B) 50% U-Gb$_3$ (C) 100% S-Gb$_3$ and (D) 100% U-Gb$_3$. Yellow spheres are the first carbon atoms of the lipids hydrophobic moiety. Gb$_3$ long chains (cyan color) interdigitate into the opposite monolayer. Also, the S-Gb$_3$ tails are highly ordered and tilted. These bilayers are not planar.
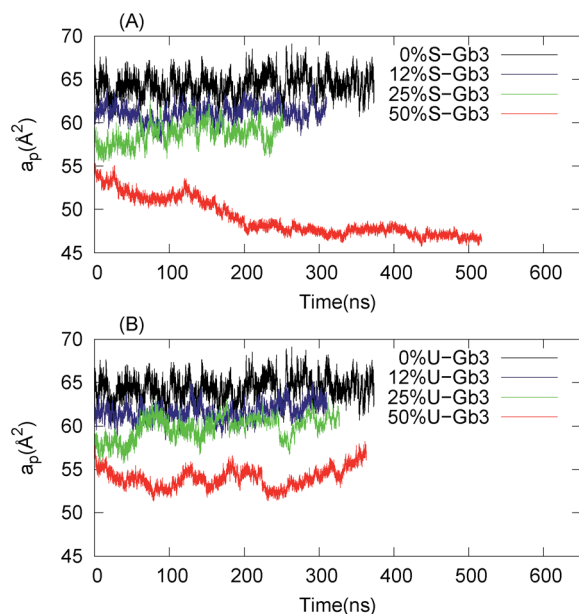
Fig. 3 Projected area per lipid ($a_p = 2L_xL_y/N$) (A) mixture contains different concentrations of S-Gb$_3$ in a DOPC lipid bilayer. (B) Mixture contains different concentrations of U-Gb$_3$ in a DOPC lipid bilayer. Data for 100% Gb$_3$ systems, were not shown, because a_p does not represent the correct area per lipid for these systems (see polynomial fitting subsection).

The very high order parameter for 50% S-Gb$_3$ indicates that this system is in an ordered phase state. The transition of this system from an initially disordered state to an ordered state can be observed from the distinct differences in the Voronoi diagrams at the beginning (Fig. 9A in the ESI†) and the end of the simulation (Fig. 9B in the ESI†). In the ordered state, many lipids acquire a very low area per lipid, depicted by dark blue colors. It is important to note that S-Gb$_3$ orders the nearby DOPC acyl chains, whereas increasing the concentration of U-Gb$_3$ only has a small effect on the DOPC lipids, even up to 50% U-Gb$_3$. The behaviour of the order parameter for the sphingosine chain of Gb$_3$ in the low concentration regime is in good agreement with previous simulations of sphingomyelin lipids.[45]

Lipid tilt

Tilt of the hydrophobic chains of lipid with respect to the bilayer normal is a characteristic parameter of the internal structure of the membrane in ordered phases. In the l$_d$ phase, the average tilt is zero in the absence of constraints which is imposed by external objects (for example proteins). Changes in the lipid tilt are associated with energy cost and coupled to the membrane bending energy.[46]

The average orientation of the lipid chains is determined by the lipid tail director vector, **n** (Fig. 5A). Deviation of **n** from the bilayer normal (**N**) is quantified by the tilt vector (**m**) which is given as:

$$\mathbf{m} = \frac{\mathbf{n}}{\mathbf{n} \cdot \mathbf{N}} - \mathbf{N} \qquad (4)$$
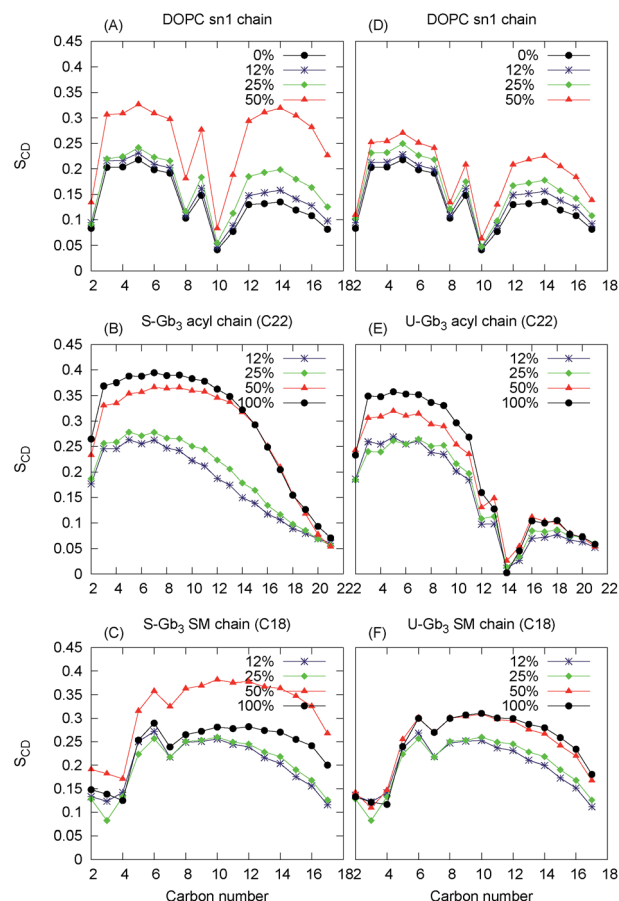

Fig. 4 Deuterium order parameter for Gb$_3$ chains and DOPC sn1 chains: left panels are for the mixture of DOPC with S-Gb$_3$ (A–C) and right pan are for the mixture of DOPC with U-Gb$_3$ (D–F).

here we define the lipid director as a unit vector pointing from the lipid interface point to its corresponding tail point where the interface point is the carbon atom which connects both tails and the tail point is the midpoint between the last carbon atoms of the two chains of each lipid.

The probability of finding a lipid with a tilt angle between θ_1 and θ_2 (in the l$_d$ phase, the tilt is independent of ϕ because of the rotational symmetry) is given by:

$$P(\theta_1, \theta_2) = \int_{\theta_1}^{\theta_2} p(\theta, \phi) \sin \theta \, \mathrm{d}\theta \, \mathrm{d}\phi \qquad (5)$$

where θ is the angle between **n** and **N**, ϕ is the azimuthal angle and $p(\theta, \phi)$ is the density of the tilt probability. In the liquid phase, the membrane energy term corresponding to the lipid tilt is (for more details see ref. 46).

$$F_{\text{tilt}} = \frac{1}{2} \int \mathrm{d}A \kappa_\theta \mathbf{m}^2 = \frac{1}{2} \int \mathrm{d}A \kappa_\theta \tan^2(\theta) \qquad (6)$$

where κ_θ is the tilt modulus. $p(\theta)$ is expected to have a form like:

$$p(\theta) \propto \exp\left(-\frac{1}{2} a_p \kappa_\theta \frac{\tan^2(\theta)}{k_B T}\right) \qquad (7)$$
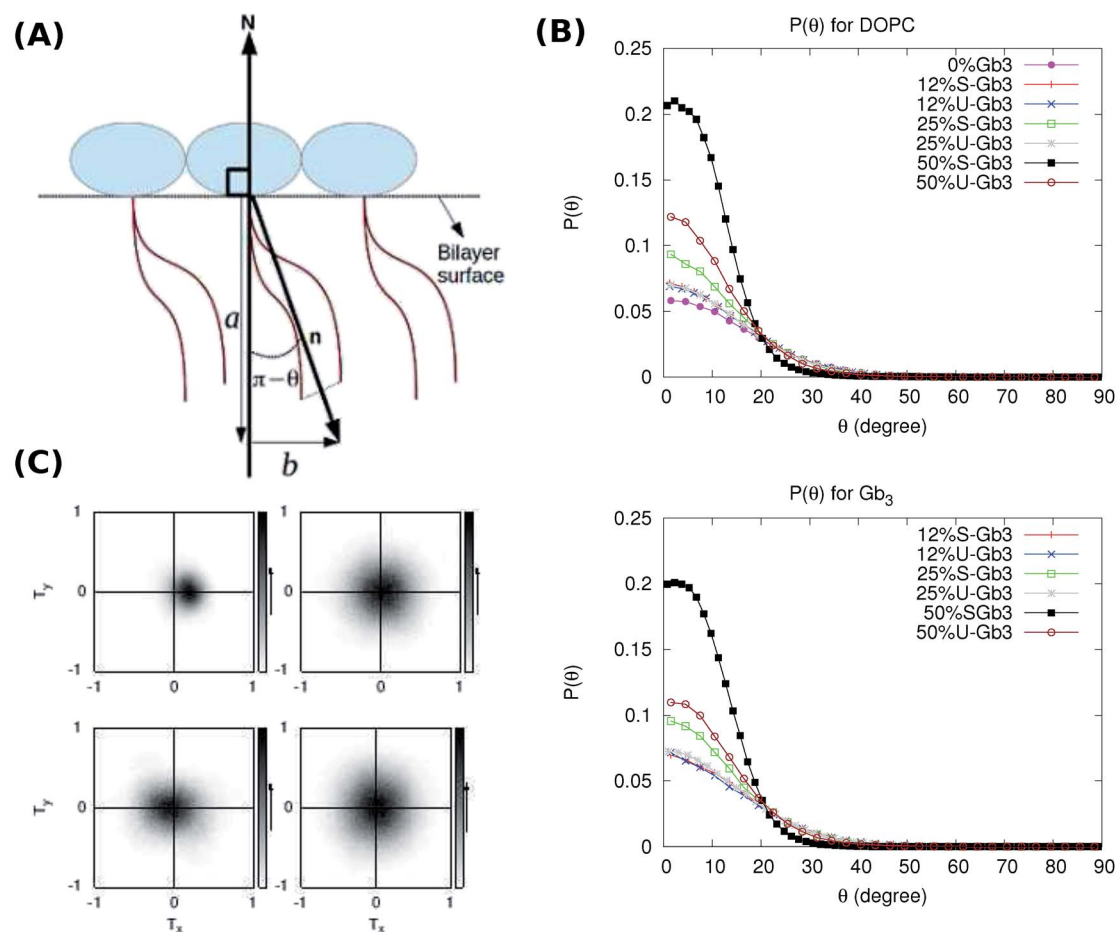
Fig. 5 (A) Director (**n**) is a unit vector along chains of a lipid and its deviation form **N** is given by tilt vector (**m**). The size of the tilt vector is equal to $\frac{|b|}{|a|}$ and is in the same direction as b. (B) Probability of lipid tilt. (Top) $p(\theta)$ for DOPC. (Bottom) $p(\theta)$ for Gb$_3$. The cyan curve for 50% S-Gb$_3$ does not peak at 0, indicating a net lipid tilt. The corresponding curve for DOPC (cyan curve, top panel) also has a non-zero maximum. (C) 2D tilt distribution map. (Left top) 50% S-Gb$_3$. (Right top) 25% S-Gb$_3$. (Left bottom) 50% U-Gb$_3$. (Right bottom) pure DOPC.

where a_p is the projected area per lipid. Eqn (7) shows that for small θ, $p(\theta)$ has a Gaussian form with a maximum value at $\theta = 0$. A deviation of the maximum from 0 indicates tilted lipids, and therefore an ordered phase.

Such a deviation, and thus an ordered phase is observed at high concentrations of S-Gb$_3$ (Fig. 5B). Also, the higher peaks of the profiles containing high percentages of S-Gb$_3$ correspond to a larger value for κ_θ and a more rigid bilayer. Thus, the increase in Gb$_3$ concentration rigidifies the bilayer, particularly for S-Gb$_3$. To further visualise the tilt in the systems, a 2D tilt distribution map of the director vector density ($\rho(T_x, T_y)$) was made. $\rho(T_x, T_y)$ was measured as the time average of the number of lipids whose director vector projection on the membrane plane is equal to $T_x\mathbf{i} + T_y\mathbf{j}$. Fig. 5C shows the 2D tilt distribution map for different systems. For 50% S-Gb$_3$, the maximum peak is a bit shifted from the center, implying an overall non-zero average tilt for the system.

Diffusion coefficient

Lipid diffusion constants for different systems were measured by evaluating the root mean-square deviation and using the Einstein

Table 4 Diffusion constant for different systems

System	DOPC μm² s⁻¹	Gb₃ μm² s⁻¹
0 Gb$_3$	5.5 ± 0.8	—
12 U-Gb$_3$	3.7 ± 0.4	3.3 ± 0.7
12 S-Gb$_3$	3.2 ± 0.5	3.0 ± 0.7
25 U-Gb$_3$	2.4 ± 0.1	2.3 ± 0.2
25 S-Gb$_3$	1.2 ± 0.2	2.0 ± 0.2
50 U-Gb$_3$	1.8 ± 0.1	1.3 ± 0.2
50 S-Gb$_3$	0.3 ± 0.1	0.4 ± 0.1
100 U-Gb$_3$	—	0.3 ± 0.2
100 S-Gb$_3$	—	0.4 ± 0.3

relationship. The values are given in Table 4. High concentrations of Gb$_3$ resulted in lower lateral diffusion coefficients of the lipid in the bilayer plane. At low concentrations, the values are close to the expected values for fluid lipid bilayers (around 8 μm² s⁻¹ for DOPC[47]). Beyond 12.5% Gb$_3$, the diffusion of DOPC is significantly lowered by S-Gb$_3$ and to a lesser degree by U-Gb$_3$.

Effects of Gb₃ fatty acid chain length disparity

The Gb$_3$ lipid has a big length mismatch in its two hydrocarbon tails. The sphingosine chain has 18 carbon atoms while the acyl chain contains 22 carbon atoms. Three different states for such a chain mismatch have been suggested, which under some conditions could lead to interdigitation between the hydrocarbons of the two opposite monolayers and drive the system in a new phase state.[48] In the mixed systems, the shorter Gb$_3$ chain (sphingosine chain) is packed end to end with DOPC chains, while the Gb$_3$ acyl chain from both the leaflets penetrate the hydrocarbon region of the opposite monolayer, more so for S-Gb$_3$ (Fig. 2). The peak in the Gb$_3$ acyl chain density profile (Fig. 6) shows interdigitation between the acyl chains of the two opposing monolayers. The higher peak of S-Gb$_3$ compared to that of U-Gb$_3$ shows that it is more favourable for S-Gb$_3$ to interdigitate into the other monolayer. Similar results are observed for lower Gb$_3$ concentrations (data not shown).

Lipid rotation

Lipid rotation around the bilayer normal is one of the slower degrees of freedom of the lipids in a lipid bilayer. The two-time correlation function for lipid rotation is defined as

$$C_\theta(t_0) = \langle R_\theta(t)R_\theta(t + t_0)\rangle \tag{8}$$

where $R_\theta(t)$ is the projection of a vector on the membrane plane, which points from the first carbon of the first chain to the first carbon of the second chain of each lipid. $\langle x \rangle$ is the ensemble average of the x. C_θ for Gb$_3$ decays very slowly compared to DOPC lipids (Fig. 7), because the Gb$_3$ lipid has a significant difference in its chain lengths that results in interdigitation. In this situation, the Gb3 lipid can rotate in two ways (1) around its principal axis: such a rotation is strongly restricted because one of the tails is interdigitated into the opposite leaflet. (2) Around its longer chain: such a rotation is also slowed down, because the axis of rotation is not along the principal axis, and the moment of inertia of the lipid increases. At high concentration of Gb$_3$, DOPC lipids are in contact with many Gb$_3$ lipids not only in the same leaflet, but also from the interdigitated C22 Gb$_3$ tails from the opposing leaflet, and this can cause DOPC to freeze. Also similar to other effects, the impact of S-Gb$_3$ is stronger than the one of U-Gb$_3$.

Phase separation and mixing of Gb₃ in a DOPC lipid bilayer

The time and length scales accessible to atomistic MD simulations are in the order of µs and 10 s of nm using present soft/
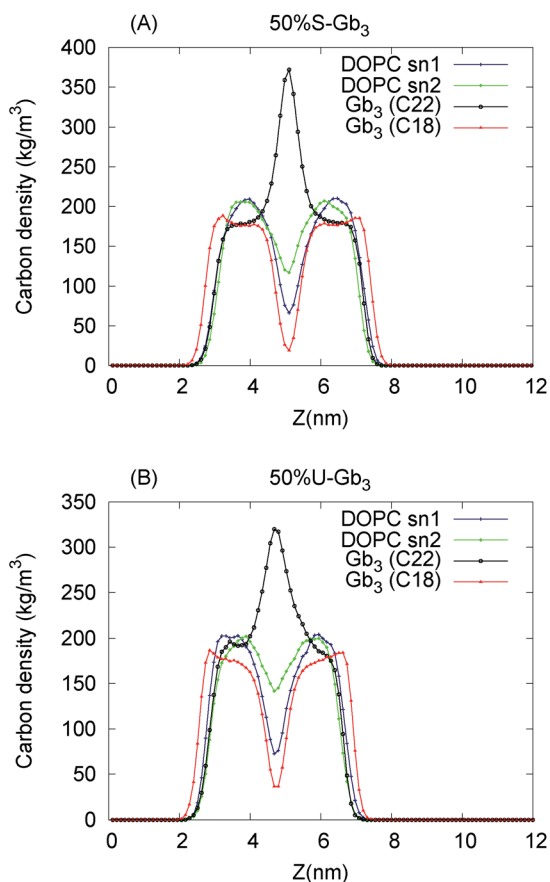

Fig. 6 Lipid fatty acid chain carbon density profile along the bilayer normal for the 50% Gb$_3$ systems (A) S-Gb$_3$ and (B) U-Gb$_3$. Gb$_3$ chain mismatch leads to interdigitation between the hydrocarbons of the two opposing monolayers. The higher peak for S-Gb$_3$ shows that it is more favourable for S-Gb$_3$ to interdigitate into the other monolayer.
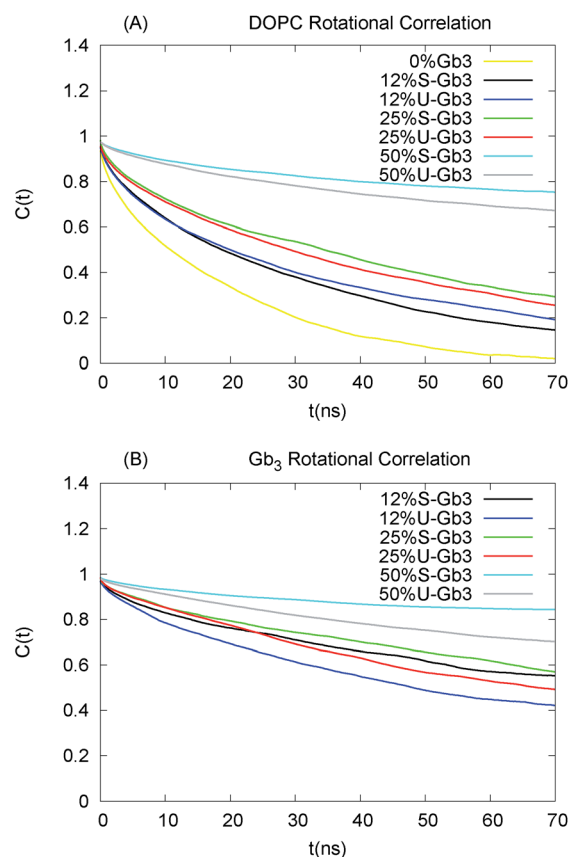

Fig. 7 Rotational correlation function: (A) C_θ for DOPC (B) C_θ for Gb$_3$. Gb$_3$ lipids rotate much more slowly than DOPC lipids, owing to the large mismatch in the two chain lengths of Gb$_3$. The longer chains thus interdigitate into the opposing leaflet (see text).

hardware. It is difficult to study the complete spontaneous phase separation of lipid mixtures without resorting to coarse-grained techniques. To deal with this, instead of waiting for the system to phase separate, a phase separated system was created and the number of mixed lipids was considered. The initial configuration contains 16 Gb$_3$ lipids (for both S-Gb$_3$ and U-Gb$_3$) in a patch embedded into one monolayer of a DOPC bilayer. The simulation was then run for 400 ns.

Two U-Gb$_3$ lipids mixed in the DOPC bilayer after 400 ns (Fig. 8B), while no mixing was observed for S-Gb$_3$ for the same simulation time (Fig. 8A). Thus, we can hypothesize from the data that U-Gb$_3$ has a higher affinity to mix with DOPC, compared to S-Gb$_3$. This effect could be because of the height mismatch between DOPC and S-Gb$_3$ (Fig. 8C and D) and/or because of unfavourable contacts between the saturated acyl chain of the S-Gb$_3$ and the unsaturated DOPC chains.

The method above does not quantify phase behaviour accurately, but does provide a comparison between the mixing rates of S-Gb$_3$ and U-Gb$_3$.

Discussion

The Gb$_3$ carbohydrate moiety, which is identical in all Gb$_3$ types, is essential for Shiga toxin binding to a cell membrane and its subsequent internalization into the host cell.[9] However, different types of Gb$_3$ behave differently in the Gb$_3$ involving processes. The most notable example is the inability of STxB to

Fig. 8 Last snapshot of the phase separated systems (16 Gb$_3$ in a DOPC lipid bilayer). After 400 ns, (A) no S-Gb$_3$ lipid is separated from the S-Gb$_3$ patch while (B) two U-Gb$_3$ lipids diffused away from the U-Gb$_3$ patch. (C) and (D) are the lateral view of (A) and (B), respectively. A height mismatch between S-Gb$_3$ and DOPC can be seen while such an effect is not present for U-Gb$_3$. The height mismatch is one of the factors leading to a lower tendency of S-Gb$_3$ to mix in the bilayer.

induce tubular membrane invagination upon binding to S-Gb$_3$ on the surface of a DOPC model membrane. On the other hand, STxB bound to U-Gb$_3$ on the surface of a DOPC model membrane induces tubular invaginations.[2,12] Thus, STxB binding to the membrane is insufficient for the formation of membrane tubular invagination and the presence of a specific Gb$_3$ species is required.

We have used all-atom MD simulations to investigate the effects of varying the Gb$_3$ concentration as well as the degree of unsaturation of its acyl chains on the physical properties of DOPC lipid bilayers. Our results reveal two important features of the Gb3 structure that strongly affect the structure and dynamics of the lipid bilayers when it is present at high concentrations. (1) The Gb$_3$ chain length mismatch results in interdigitation of the longer chain into the opposite monolayer and in subsequent reduction in lipid fatty acid chain fluctuations, and ordering of all bilayer chains. The effect is stronger for S-Gb$_3$ compared to U-Gb$_3$. (2) The degree of Gb$_3$ acyl chain saturation influences the affinity of Gb$_3$ lipids to mix or demix in DOPC lipid bilayers.

The Gb$_3$ concentration is low in the experiments (up to 10%).[2,12] However, considering that each STxB molecule can bind up to 15 Gb$_3$ lipids, it is reasonable to think that the Gb$_3$ concentration is high (up to 40%) under the protein. Combining this assumption with the fact that STxB proteins cluster on the surface of a membrane,[2,11] a high concentration of Gb$_3$ is expected in the domains enriched by STxB that modifies the local bilayer structure. This argument and the simulation results provide the following insights into several experimental observations:

(a). Binding of STxB to a bilayer containing S-Gb$_3$ and DOPC does not drive the membrane to invaginate:[2] we hypothesise that invagination will not occur when STxB is bound to an ordered phase. A high energetic cost must be borne to bend such a rigid bilayer which cannot be compensated by the system. Such an ordered and rigid bilayer is observed at a high concentration of S-Gb$_3$ in our simulations, as shown in Fig. 5. A similar l_o phase is present in a phase-separated lipid bilayer composed of DOPC, sphingomyelin, cholesterol and porcine Gb$_3$. Binding of STxB to the l_o phase of this membrane does not induce tubular invagination.[11] On the other hand, U-Gb$_3$ does not form a rigid bilayer, and thus membrane invagination can occur without incurring the high bending energy penalty. Experiments also show that tubular invagination is observed upon STxB binding to a membrane containing only DOPC and U-Gb$_3$, which does not exhibit the l_o phase.[11]

(b). For lipid bilayers containing DOPC, sphingomyelin, cholesterol and Gb$_3$-C24 : 0, which are phase separated at room temperature, no change in the area percentage of the l_o phase was observed upon STxB binding experimentally:[13] we have shown that S-Gb$_3$ tends to remain phase separated in such a DOPC bilayer. Thus, SGb$_3$ is probably already in a phase separated state in the mixed bilayer even before STxB binds. Thus, STxB binds to the l_o phase, and no further changes occur in the system.

(c). Increase in membrane height due to protein clustering:[11] Table 3 shows that the membrane thickness increases with
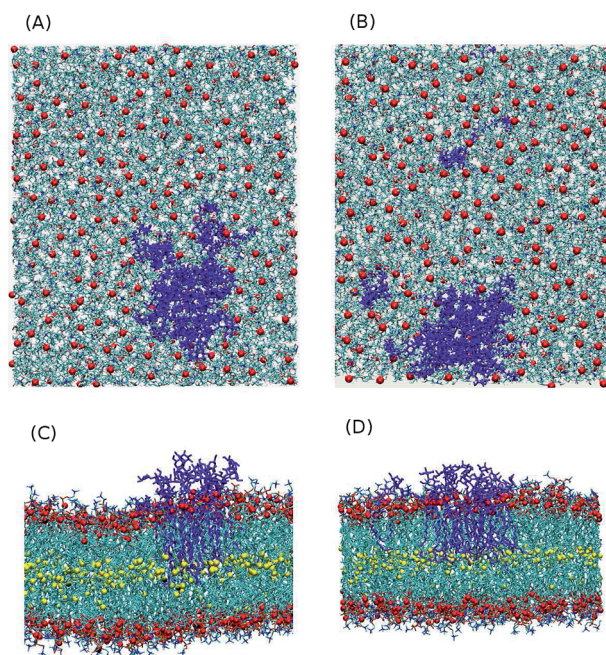
increasing Gb$_3$ concentration. The change is particularly significant at high S-Gb$_3$ concentrations.

(d). The condensation of phospholipid–Gb3 monolayers at high Gb3 concentrations:[16] increasing the Gb$_3$ concentration induces a progressively lower area per lipid and a dramatic reduction was observed at high S-Gb$_3$ concentrations (Table 3). In the experiments a similar impact for S-Gb$_3$ was observed.[16]

Our results suggest that the STxB binding to a lipid bilayer indirectly influences the properties of the lipid bilayer by clustering and accumulating Gb$_3$ underneath the protein aggregate. Invagination is not induced when Gb$_3$ is saturated, because S-Gb$_3$ forms a rigid immobile phase resistant to bending whilst the unsaturated version does not. Our results provide several hypotheses which can resolve some of the unexplained experimental observations with regard to the phenomenon of membrane invagination induced by Shiga toxins. Further investigation is needed to validate these hypotheses.

Acknowledgements

References

1 B. Maggio, M. L. Fanani, C. M. Rosetti and N. Wilke, *Biochim. Biophys. Acta*, 2006, **1758**, 1992–1944.

2 W. Römer, L. Berland, V. Chambon, K. Gaus, B. Windschiegl, D. Tenza, M. Aly, V. Fraisier, J. Florent, D. Perrais, C. Lamaze, G. Raposo, C. Steinem, P. Sens, P. Bassereau and L. Johannes, *Nature*, 2007, **450**, 670–675.

3 T. Eierhoff, B. Bastian, R. Thuenauer, J. Madl, A. Audfray, S. Aigal, S. Juillot, G. Rydell, S. Muller, S. de Bentzmann, A. Imberty, C. Fleck and W. Romer, *Proc. Natl. Acad. Sci. U. S. A.*, 2014, **111**, 12895–12900.

4 O. Kovbasnjuk, R. Mourtazina, B. Baibakov, T. Wang, C. Elowsky, M. A. Choti, A. Kane and M. Donowitz, *Proc. Natl. Acad. Sci. U. S. A.*, 2005, **102**, 19097–19092.

5 L. Johannes and D. Decadin, *Gene Ther.*, 2005, **12**, 1360–1368.

6 F. Sandoval, M. Terme, M. Nizard, C. Badoual, M. Bureau, L. Freyburger, O. Clement, E. Marcheteau, A. Gey, G. Fraisse, C. Bouguin, N. Merillon, E. Dransart, T. Tran, F. Quintin-Colonna, G. Autret, M. Thiebaud, F. Suleman, S. Riffault, T. Wu, O. Launay, C. Danel, J. Taieb,

7 J. Richardson, L. Zitvogel, W. Fridman, L. Johannes and E. Tartour, *Sci. Transl. Med.*, 2013, **5**, 172ra20.

7 H. Pere, Y. Montier, J. Bayry, N. Merillon, F. Quintin-Colonna, E. Dransart, C. Badoual, A. Gey, P. Ravel, F. Sandoval, C. Guerin, O. Adotevi, Y. Lone, L. Ferreira, B. Nelson, D. Hanahan, W. Fridman, L. Johannes* and E. Tartour*, *Blood*, 2011, **118**, 4853–4862.

8 O. Adotevi, B. Vingert, L. Freyburger, P. Shrikant, Y. Lone, F. Quintin-Colonna, N. Haicheur, M. Amessou, A. Herbelin, P. Langlade-Demoyen, W. Fridman, F. Lemonnier, L. Johannes* and E. Tartour*, *J. Immunol.*, 2007, **179**, 3371–3379.

9 H. Ling, A. Boodhoo, B. Hazes, M. D. Cummings, G. D. Armstrong, J. L. Brunton and R. J. Read, *Biochemistry*, 1998, **37**, 1777–1788.

10 D. G. Pina, L. Johannes and M. A. Castanho, *Biochim. Biophys. Acta*, 2007, **1768**, 628–636.

11 B. Windschiegl, A. Orth, W. Römer, L. Berland, B. Stechmann, P. Bassereau, L. Johannes and C. Steinem, *PLoS One*, 2009, **4**, e6238.

12 M. Safouane, L. Berland, A. Callan-Jones, B. Sorre, W. Römer, L. Johannes, G. E. S. Toombes and P. Bassereau, *Traffic*, 2010, **11**, 1519–1529.

13 O. M. Schütte, A. Ries, A. Orth, L. J. Patalag, W. Römer, C. Steinem and D. B. Werz, *Chem. Sci.*, 2014, **5**, 3104–3114.

14 D. J. Chinnapen, W. Hsieh, Y. te Welscher, D. Saslowsky, L. Kaoutzani, E. Brandsma, L. D'Auria, H. Park, J. Wagner, K. Drake, M. Kang, T. Benjamin, M. Ullman, C. Costello, A. Kenworthy, T. Baumgart, R. Massol and W. Lencer, *Dev. Cell*, 2012, **23**, 573–586.

15 V. Solovyeva, L. Johannes and A. C. Simonsen, *Soft Matter*, 2015, **11**, 186–192.

16 E. B. Watkins, H. Gao, A. J. C. Dennison, N. Chopin, B. Struth, T. Arnold, J.-C. Florent and L. Johannes, *Biophys. J.*, 2014, **107**, 1146–1155.

17 H. J. C. Berendsen, D. van der Spoel and R. van Drunen, *Comput. Phys. Commun.*, 1995, **91**, 43–56.

18 E. Lindahl, B. Hess and D. van der Spoel, *J. Mol. Model*, 2001, **7**, 306–317.

19 D. van der Spoel, E. Lindahl, B. Hess, G. Groenhof, A. E. Mark and H. J. C. Berendsen, *J. Comput. Chem.*, 2005, **26**, 1701–1718.

20 B. Hess, C. Kutzner, D. van der Spoel and E. Lindahl, *J. Chem. Theory Comput.*, 2008, **4**, 435–447.

21 P. Bjelkmar, P. Larsson, M. A. Cuendet, B. Hess and E. Lindahl, *J. Chem. Theory Comput.*, 2010, **6**, 459–466.

22 J. B. Klauda, R. M. Venable, J. A. Freites, J. W. O'Connor, D. J. Tobias, C. Mondragon-Ramirez, I. Vorobyov, A. D. MacKerell Jr and R. W. Pastor, *J. Phys. Chem. B*, 2010, **114**, 7830–7843.

23 W. L. Jorgensen, J. Chandrasekhar, J. D. Madura, R. W. Impey and M. L. Klein, *J. Chem. Phys.*, 1983, **79**, 926–935.

24 A. D. MacKerell Jr, D. Bashford, M. Bellott, J. R. L. Dunbrack, J. D. Evanseck, M. J. Field, S. Fischer, J. Gao, H. Guo, S. Ha, D. Joseph-McCarthy, L. Kuchnir, K. Kuczera, F. T. K. Lau, C. Mattos, S. Michnick, T. Ngo, D. T. Nguyen, B. Prodhom,

W. E. R. III, B. Roux, M. Schlenkrich, J. C. Smith, R. Stote, J. Straub, M. Watanabe, J. Wiórkiewicz-Kuczera, D. Yin and M. Karplu, *J. Phys. Chem. B*, 1998, **102**, 3586–3616.

25 H. J. C. Berendsen, J. P. M. Postma, A. DiNola and J. R. Haak, *J. Phys. Chem. B*, 1984, **81**, 3684–3690.

26 W. G. Hoover, *Phys. Rev. A*, 1985, **31**, 1695–1697.

27 B. Hess, H. Bekker, H. J. C. Berendsen and J. G. E. M. Fraaije, *J. Comput. Chem.*, 1997, **18**, 1463–1472.

28 M. Parrinello and A. Rahman, *J. Appl. Phys.*, 1981, **52**, 7182–7190.

29 S. Noséa and M. Klein, *Mol. Phys.*, 1983, **50**, 1055–1076.

30 H. J. C. Berendsen, J. P. M. Postma, A. DiNola and J. R. Haak, *J. Chem. Phys.*, 1984, **81**, 3684–3690.

31 O. Guvench, S. Greene, G. Kamath, J. Brady, R. Venable, R. Pastor and A. J. MacKerell, *J. Comput. Chem.*, 2008, **29**, 2543–2564.

32 O. Guvench, E. R. Hatcher, R. M. Venable, R. W. Pastor and A. J. MacKerell, *J. Chem. Theory Comput.*, 2009, **5**, 2353–2370.

33 E. P. Raman, O. Guvench and A. J. MacKerell, *J. Phys. Chem. B*, 2010, **114**, 12981–12994.

34 O. Guvench, S. S. Mallajosyula, E. P. Raman, E. Hatcher, K. Vanommeslaeghe, T. J. Foster, F. W. Jamison and A. J. MacKerell, *J. Chem. Theory Comput.*, 2011, **7**, 3162–3180.

35 S. S. Mallajosyula and A. J. MacKerell, *J. Phys. Chem. B*, 2011, **115**, 11215–11229.

36 C. M. Breneman and K. B. Wiberg, *J. Comput. Chem.*, 1990, **11**, 361–373.

37 M. J. Frisch, G. W. Trucks, H. B. Schlegel, G. E. Scuseria, M. A. Robb, J. R. Cheeseman, G. Scalmani, V. Barone, B. Mennucci, G. A. Petersson, H. Nakatsuji, M. Caricato, X. Li, H. P. Hratchian, A. F. Izmaylov, J. Bloino, G. Zheng, J. L. Sonnenberg, M. Hada, M. Ehara, K. Toyota, R. Fukuda, J. Hasegawa, M. Ishida, T. Nakajima, Y. Honda, O. Kitao, H. Nakai, T. Vreven, J. A. Montgomery Jr, J. E. Peralta, F. Ogliaro, M. Bearpark, J. J. Heyd, E. Brothers, K. N. Kudin, V. N. Staroverov, R. Kobayashi, J. Normand, K. Raghavachari, A. Rendell, J. C. Burant, S. S. Iyengar, J. Tomasi, M. Cossi, N. Rega, J. M. Millam, M. Klene, J. E. Knox, J. B. Cross, V. Bakken, C. Adamo, J. Jaramillo, R. Gomperts, R. E. Stratmann, O. Yazyev, A. J. Austin, R. Cammi, C. Pomelli, J. W. Ochterski, R. L. Martin, K. Morokuma, V. G. Zakrzewski, G. A. Voth, P. Salvador, J. J. Dannenberg, S. Dapprich, A. D. Daniels, Ö. Farkas, J. B. Foresman, J. V. Ortiz, J. Cioslowski and D. J. Fox, *Gaussian-09 Revision D.01*, Gaussian Inc, Wallingford CT, 2009.

38 J. P. M. Jambeck and A. P. Lyubartsev, *J. Chem. Theory Comput.*, 2012, **8**, 2938–2948.

39 N. Kučerka, J. F. Nagle, J. N. Sachs, S. E. Feller, J. Pencer, A. Jackson and J. Katsaras, *Biophys. J.*, 2008, **95**, 2356–2367.

40 J. Pan, S. Tristram-Nagle, N. Kučerka and J. F. Nagle, *Biophys. J.*, 2008, **94**, 117–124.

41 N. Kučerka, S. Tristram-Nagle and J. F. Nagle, *J. Membr. Biol.*, 2005, **208**, 193–202.

42 G. Lukat, J. Krüger and B. Sommer, *J. Chem. Inf. Model.*, 2013, **53**, 2908–2925.

43 J. Seelg, *Q. Rev. Biophys.*, 1977, **3**, 353–418.

44 J. Douliez, A. Léonard and E. J. Dufourc, *Biophys. J.*, 1995, **68**, 1727–1739.

45 J. Aittoniemi, P. S. Niemelä, M. T. Hyvönen, M. Karttunen and I. Vattulainen, *Biophys. J.*, 2007, **92**, 1125–1137.

46 M. Hamm and M. M. Kozlov, *Eur. Phys. J. E*, 2000, **3**, 323–335.

47 G. Lindblom and G. Orädd, *Biochim. Biophys. Acta*, 2009, **1788**, 234–244.

48 I. W. Levin, T. E. Thompson, Y. Barenholz and C. Huang, *Biochemistry*, 1985, **24**, 6282–6286.